The Virtual Propulsion Expert: Application of a Hybrid Surrogate-Based Rubber Engine Model in Aircraft Design

J. Häßy*
Institute of Propulsion Technology, German Aerospace Center (DLR), Cologne, Germany

B. Fröhler†
Institute of System Architectures in Aeronautics, German Aerospace Center (DLR), Hamburg, Germany

An aircraft is a complex system of systems. The engine, as a subsystem, strongly influences the design of other subsystems in a complex interplay by its performance characteristics, dimensions and mass. The ability to reliably model the overall aircraft and to find optimal designs within a short period of time is critical in the conceptual design phase to provide the basis for sound decision making. However, this is difficult to achieve since simplified engine models may lead to unreasonable results and more sophisticated models usually require the consultation of a propulsion expert. Therefore, a hybrid surrogate-based rubber engine approach is demonstrated that facilitates the exchange of disciplinary knowledge and enables the convenient integration of detailed engine models into multidisciplinary processes for overall aircraft design. A rubberized generic geared turbofan with an entry into service in 2035 is created to equip a long-haul, wide-body aircraft with different suitably sized engines from a multidimensional design space. In order to generate the training data for the surrogate-based rubber engine model, a multidisciplinary process for conceptual engine design is employed, which combines a multi point thermodynamic cycle analysis with flow path sizing, a basic aerodynamic analysis of turbomachinery, mass estimation on the level of single engine parts and a model to predict engine emissions. With the rubber engine model integrated into the aircraft design process, the off-design performance of individual engines is provided on-demand via tabulated maps, which are calculated in-the-loop. For a long-haul aircraft configuration, a bypass ratio of 14 is identified as optimal in terms of mission fuel considering snow ball effects. For growing bypass ratios, the thrust lapse increases leading to higher combustor inlet temperature and pressure at cruise operation. As a result, nitrogen oxide emissions increase with BPR for an assumed rich-burn quick-quench lean-burn (RQL) combustor and counteract savings in carbon dioxide and water emissions leading to minimum climate impact for a bypass ratio of 11. The minimum direct operating costs are realized for a bypass ratio of 12.

I. Nomenclature

ATR	=	average temperature response
BPR	=	bypass ratio
CPACS	=	common parametric aircraft configuration scheme
CR	=	cruise
DLRp2	=	DLR performance program
DOC	=	direct operating costs
ΔT_{ISA}	=	deviation from outer air temperature
EI	=	emission index
EIS	=	entry into service
EOF	=	end of field
FAR	=	fuel-to-air ratio
FL	=	flight level
GTlab	=	gas turbine laboratory

*Research Engineer, Institute of Propulsion Technology, Linder Hoehe, 51147 Cologne, Germany, Jannik.Haessy@dlr.de
†Research Engineer, Institute of System Architectures in Aeronautics, Hein-Saß-Weg 22, 21129 Hamburg, Germany, Benjamin.Froehler@dlr.de

LoD = lift-to-drag ratio
MCL = maximum climb
MDAO = multidisciplinary design analysis and optimization
MTO = maximum take-off
MTOM = maximum take-off mass
NOx = nitrogen oxides
nvPM = non-volatile particulate matter
OAD = overall aircraft design
OEM = operating empty mass
OPR = overall pressure ratio
RCE = remote component environment
RQL = rich-burn quick-quench lean-burn
SLS = sea level static
TLARs = top-level aircraft requirements
TOC = top of climb
TSFC = thrust specific fuel consumption
T_3 = outlet temperature of high pressure compressor
T_4 = combustor outlet temperature
T_{41} = stator outlet temperature of high pressure turbine
VGVs = variable inlet guide vanes
2ndSeg = second segment

II. Introduction

A. Motivation

The isolated design of a propulsion system or an airframe requires a highly complex, multidisciplinary and collaborative process. Bringing both together increases the complexity of a design challenge even further. Regardless whether the main interest lies on the propulsion system or the airframe, knowledge in the other field is of major importance in order to yield an optimal aircraft design in terms of overall system performance. For conceptual aircraft design, it is essential to reliably model the entire aircraft while being capable of exploring a large design space in a short period of time to identify potential design limits and improve decision making. However, this is difficult to achieve since simplified engine models or the unexperienced use of design tools may lead to unreasonable results and more sophisticated models usually require the consultation of a propulsion expert. In addition, it is a challenging task to find an optimally designed propulsion system. Not only the thrust requirements have to be met during all flight regimes without exceeding thermal and mechanical limits but also geometrical constraints regarding the installation of the propulsion system have to be considered. Furthermore, the dimensions, mass and fuel consumption of the propulsion system affect e.g. the drag, required lift and structural design of the overall aircraft as well as the fuel mass required for a flight mission. Changing airframe specifications in turn impact the engine thrust requirements and may affect the selection of the thermodynamic cycle which finally leads to a highly coupled design process. Typically, the knowledge for aircraft design on a conceptual level, including engine design, is distributed among various aircraft and engine manufacturers or research institutions. In order to find the optimal design, the exchange of disciplinary knowledge is necessary but difficult to achieve due to the variety of heterogeneous stakeholders. Therefore, innovative approaches are needed to integrate detailed disciplinary knowledge with respect to propulsion into processes for overall aircraft design (OAD).

B. State of the Art

Different concepts exist in the literature to integrate conceptual engine design into OAD. Here, these concepts are classified into the categories: 'scaling-based', 'direct-integration' and 'surrogate-based'. The 'scaling-based' concepts use a fixed characteristic of a reference engine, e.g. a tabulated engine performance map, that is altered during aircraft design by applying simple scaling or correction laws. Representative examples for this category can be found in [1–8]. The model validity decreases due to scaling or correction. In addition, the used reference was designed for a specific set of requirements and has a certain thermodynamic cycle. Changing thermodynamic cycle parameters is not possible

with a 'scaling-based' approach.

The approaches grouped into the category 'direct-integration' couple many disciplinary tools directly by organizing them in a multidisciplinary workflow and linking in- and outputs. Representative references for 'direct-integration' strategies are [9–15]. Multidisciplinary processes for the overall system, composed of individual process chains for the detailed design of all subsystems, offer the advantage of high flexibility and reusability. However, these processes are complex, computationally expensive and require comprehensive knowledge and experience at usage in order to avoid mistakes and errors. Furthermore, the provision of subsystem process chains requires sharing of all involved tools which is usually not possible due to intellectual property concerns of single stakeholders. Also system portability may be a challenge.

The concepts of the 'surrogate-based' category separate the phases engine design and engine selection: in a pre-processing step various engine designs are generated to populate a predefined design space that is spanned by engine requirements and major design parameters. Based on this data, surrogate models are fitted and integrated into the OAD process as a substitute of the sub-process for engine design. The surrogate-based engine representation enables the selection of different suitably sized engine designs. For example, Lammen et al. [16] presented a surrogate-based rubber engine model that allows the selection of different thermodynamic cycles and provides off-design performance for single predefined operating points. Seitz et al. [17] created a purely surrogate-based rubber engine model that can provide the continuous operational performance over the flight envelope for each engine individually. Häßy et al. [18], author of this paper, presented a concept for a hybrid surrogate-based approach that combines aspects of 'direct-integration' with a 'surrogate-based' concept. This hybrid concept uses surrogate models to store design information for a range of different engine designs. When a specific design is selected, the corresponding information is transferred to an embedded tool for thermodynamic cycle analysis that enables the calculation of off-design performance on demand. Recently, Di Stasio et al. [19] published an approach that uses surrogate models to predict engine performance at single predefined operating conditions to subsequently scale a reference engine map.

C. Objectives and Research Questions

The purpose of this publication is to present the application of the hybrid surrogate-based rubber engine approach that was proposed by Häßy et al. in [18]. Therefore, a rubberized generic geared turbofan with an entry into service in 2035 is integrated into a collaborative workflow for OAD to equip a long-haul, wide-body aircraft with different suitably sized engines from a multidimensional design space. With this work, the following research questions are addressed:

1) How can comprehensive disciplinary expertise be conveniently integrated into a multidisciplinary workflow for OAD in order to find the optimal propulsion system?
2) What is the optimal bypass ratio (BPR) in terms of mission fuel burn for a geared turbofan powering a long-haul, wide-body aircraft with entry into service (EIS) in 2035? How do the counteracting trends of thrust specific fuel consumption and parasitic aerodynamic losses due to larger dimensions and additional mass evolve with the BPR?
3) How does the selection of the BPR affects the emission of nitrogen oxides (NOx) and non-volatile particulate matter (nvPM) respectively soot? Which BPR is optimal in terms of climate impact?
4) How does the BPR influence direct operating costs (DOC)?

III. Methodology

A. Rubber Engine Concept

A hybrid surrogate-based rubber engine approach is employed according to the description in [18] and as depicted in Fig. 1. The model is created in a pre-processing step, separating engine design and engine selection. During the model creation phase, different engine designs are generated to populate a predefined design space using a certain sampling strategy. The multi-dimensional design space is spanned by requirements arising from OAD, e.g. the thrust demand at sizing operating conditions, and by important engine design parameters, e.g. the bypass ratio. Therefore, a multidisciplinary engine design process is required that provides information on e.g. thermodynamics, geometry, mass and center of gravity. Based on the generated sample set, surrogate models are trained to predict the characteristic engine parameters. In the application phase, the rubber engine model enables the selection of a specific engine from the covered continuous design space for a given set of input parameter values. The surrogate models are then evaluated with these input values. The outputs of the surrogate models are grouped into two categories: The first category

comprises engine parameters that are constant for a specific engine design and are independent of the operating state of the engine, e.g. dimensions, mass, center of gravity. When an engine is selected, the rubber engine model provides these parameters directly after surrogate model evaluation at the model interface (cf. Fig. 1). The second category includes a set of thermodynamic design parameters that uniquely define each engine and its operational limits for different ratings, e.g. bypass ratio, pressure ratios, efficiencies, maximum temperatures. Parameters of the second category are internally transferred after surrogate evaluation to initialize an embedded tool for thermodynamic cycle analysis. With this tool the off-design performance of the selected engine is calculated on-demand during application in OAD. Not only the performance of single operating points given by a set of flight conditions and a power setting can be calculated in-the-loop but also engine performance maps considering different ratings and the corresponding thermal and mechanical limits as well as power and bleed off-takes. The thermodynamic data is internally passed to an embedded model for emission calculation which provides engine emissions corresponding to engine performance at the rubber engine model interface.

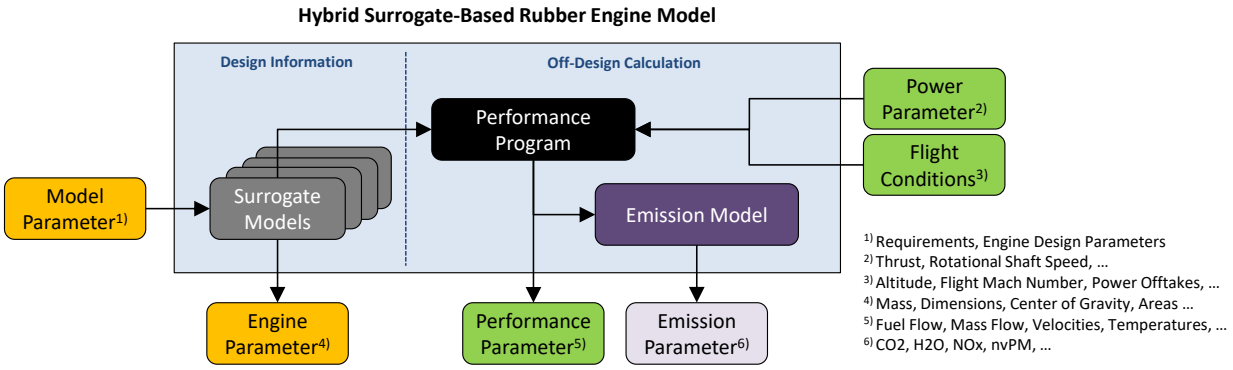

Fig. 1 Hybrid surrogate-based rubber engine model concept.

Applied in the OAD context, the rubberized engine enables the consideration of detailed interactions between the airframe and propulsion unit based on sophisticated, approved models. To achieve this, the complexity of the OAD process is not drastically increased due to the encapsulation of engine design in a preprocessing step. The hybrid surrogate-based approach is suitable whether the propulsion system architecture is a conventional turbofan engine or is based on a disruptive concept. A high degree of standardization and reusability can be achieved by using an abstract interface of the rubber engine model and a common language for data exchange. Thereby, the design of overall systems is accelerated and optimal design decisions are enabled based on fast and standardized transfer of complex knowledge without sharing complex process chains.

B. Engine Design Process

The hybrid surrogate-based rubber engine concept will be demonstrated for a generic unmixed geared turbofan engine with EIS = 2035. In order to generate the training data for the surrogate-based rubber engine model, an iterative process for conceptual design is set up using the virtual propulsion framework GTlab (Gas Turbine Laboratory) [20–22]. The multidisciplinary design process combines a multi point thermodynamic cycle analysis with a knowledge-based method for flow path sizing [23], a basic aerodynamic analysis of turbo machinery [24], mass estimation on the level of single engine parts [23] and a model for the prediction of engine emissions. The dependencies between different disciplines in the conceptual engine design process are depicted by means of a flow chart in Fig. 2.

All disciplinary models are initialized based on the characteristics of a reference engine. For this paper, the reference is a generic unmixed geared turbofan model similar to the Pratt & Whitney PW1100G with EIS = 2016. The conceptual engine design process is calibrated using publicly available data of the existing engine [25–27] and then the reference model is scaled up to reach the targeted thrust category of a long-haul aircraft configuration. In order to account for technological improvements for an entry into service in the year 2035, assumptions are introduced, e.g. for temperature limits, fan flow capacity, cooling air demand and turbo machinery efficiencies. In the following, the respective models and assumptions are briefly described.

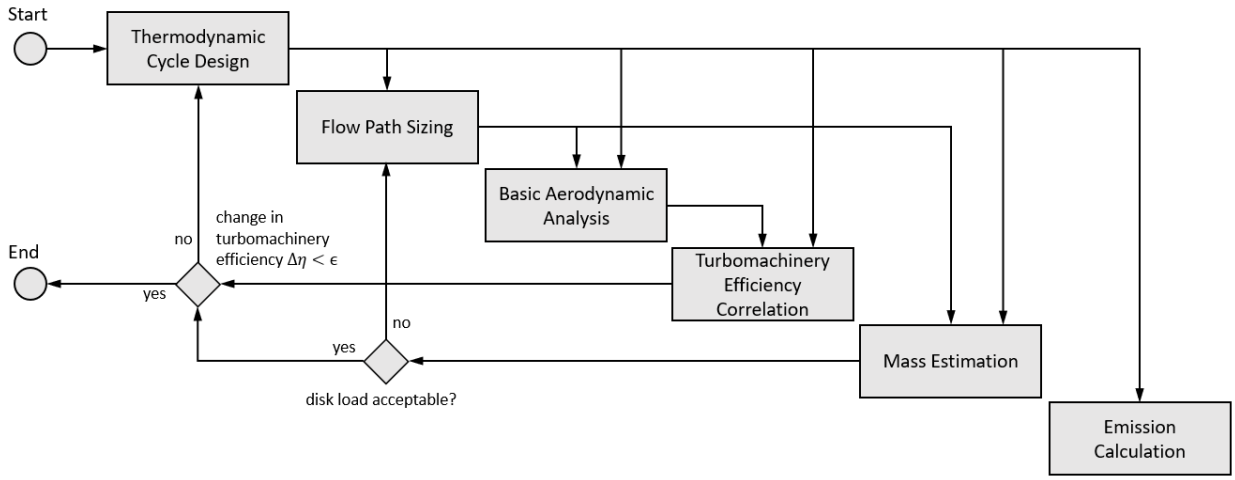

Fig. 2 Flow chart of the engine conceptual design process.

Thermodynamic Cycle

Engine performance is calculated with the program DLRp2 (DLR Performance Program), which is part of the GTlab framework. The schematic of the used engine performance model is shown in figure 3. The thermodynamic model considers relevant sizing operating points in a multi design point approach. In the high-speed regime, cruise (CR) and top of climb (TOC) are taken into account. For low-speed operation, maximum take-off (MTO) at sea level static (SLS) as well as end of field (EOF) and second segment (2ndSeg) with one engine inoperative are considered. Design laws are implemented to ensure feasible engine cycles that comply with requirements and the thermodynamic cycle is iteratively adjusted until the assumed technological limits are met. Exemplary thermodynamic cycle data is given in table 1 for BPR = 14.

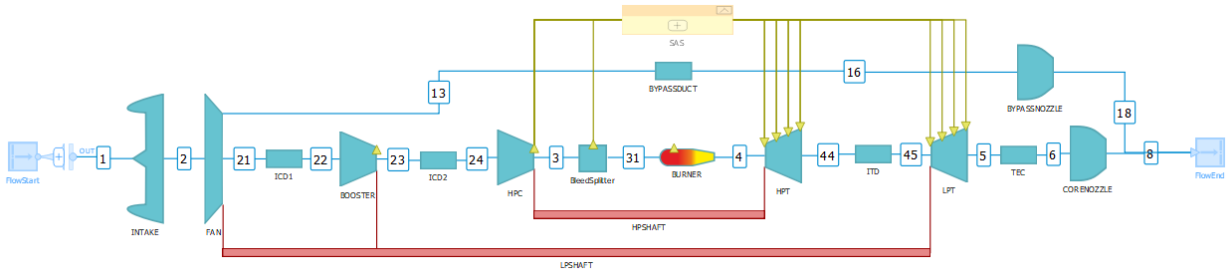

Fig. 3 Schematic of the engine performance model.

- The overall pressure ratio is adjusted until the maximum outlet temperature of the compressor section reaches T_3 = 1000 K. Depending on the thrust requirements, this limit is reached either for MTO-SLS, EOF or 2ndSeg. Additionally, the blade height of the last compressor stage is required to be at least 13 mm. However, the blade height limit is not critical for the herein considered thrust category.
- The fuel-to-air ratio is adjusted to reach a stator outlet temperature of the first high-pressure turbine stage (T_{41}) either at TOC with T_{41} = 1725 K (MCL Rating) or at a low-speed operating condition with T_{41} = 2050 K (MTO Rating) depending on which case is more critical.
- The cooling air demand for high-pressure turbine stages is modelled according to a correlation of Grieb [28]. The relative cooling air demand relates the mass flow of cooling air to the inlet mass flow into the stage and is modelled as a function of the cooling air temperature and the stator outlet temperature. For EIS = 2035, it is assumed that shell and spar stator blades using ceramic matrix composites [29] reduce the relative cooling air demand for the first and second stage by 5 and 2 %-points, respectively.

- The maximum flow capacity of the fan is set to 218 [kg/s/m^2] and is either reached at TOC, EOF or 2ndSeg. The specification of flow capacity defines the Mach number at the fan inlet plane.
- The fan pressure ratio is adjusted to reach the ideal nozzle velocity ratio of an unmixed turbofan engine, which equals the transmission efficiency. Meeting this conditions ensures an optimal thrust split between the bypass and core nozzle.
- The pressure loss in the bypass duct is modelled as a function of the duct inlet Mach number. The used correlation was deduced from CFD analysis of a representative geometry for a high-bypass engine.
- Design values for turbo component efficiencies at cruise are set based on a simplified aerodynamic analysis and a semi-empirical correlation for turbomachinery (cf. III.B). Off-design efficiencies are predicted by means of generic component maps.To account for varying inlet conditions in dependence on the flight altitude, a correction is applied based on the Reynolds number index.

Table 1 Thermodynamic cycle data for BPR = 14.

Parameter	**Unit**	Cruise	Top of Climb	Max. Take-off	End Of Field	2nd Segment
Flight Mach Number	[-]	0.83	0.81	0.00	0.24	0.24
Flight Altitude	[m]	10924	10058	0	11	122
ΔT_{ISA}	[K]	0	10	15	15	15
Thrust	[kN]	45.4	56.6	314.1	225.7	243.5
Fan Inlet Mach Number	[-]	0.66	0.68	0.58	0.58	0.61
Fan Pressure Ratio	[-]	1.38	1.40	1.39	1.37	1.40
BPR	[-]	14.00	13.18	13.09	13.56	13.27
OPR	[-]	52.7	57.4	51.4	49.4	53.0
T_3	[K]	829	901	984	981	1000
T_{41}	[K]	1597	1725	1910	1897	1942
TSFC	[g/kNs]	14.41	14.91	6.62	9.12	9.16

Flow Path Sizing

A knowledge-based approach for flow path sizing as described by Häßy et al. [23] is applied to establish the engine geometry. Dimensionless characteristic information on single turbo components are extracted from the general arrangement of the PW1100G published in [27]. These geometrical characteristics are used in combination with the calculated thermodynamic cycle data to predict the geometry of single turbo components. Then, the component geometries are arranged to form the overall engine flow path and spool speeds are determined. The flow path for BPR = 14 is exemplary shown in figure 4.

- The Mach numbers at the inlet and outlet of each turbo component are held constant for cruise operation. By specifying Mach numbers, the flow areas can be calculated for a given mass flow and thermodynamic fluid state.
- The radial location of components is calculated based on constant hub-to-tip or mean-line radius ratios.
- The blade geometry is established with constant aspect ratios, taper ratios and relative gaps as well as the extracted mean-line and annulus height characteristic of the reference.
- The number of compressor stages is selected to keep the aerodynamic loading limited. The high- and low-pressure turbines are assumed to have two and four stages, respectively. Less stages for the low-pressure turbine would be possible with respect to aerodynamic loading but will degrade efficiency to an unacceptable degree for high BPRs.
- The length of the nacelle is set by the core engine since the relative location of the bypass nozzle with respect to the low-pressure turbine is maintained. The thickness of the nacelle is scaled with its length.
- The rotational speed of the fan is determined by a correlation of Grieb [28] that relates the reduced circumferential tip speed to the fan pressure ratio. The rotational speed of the high- and low-pressure shafts is set to reach a maximum allowed blade pull stress of the turbines. Then, the fan and low-pressure shaft speeds define the gear ratio.

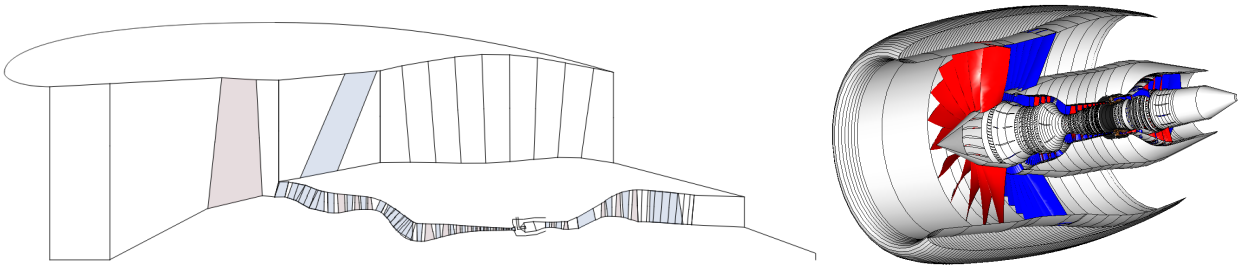

Fig. 4 Exemplary flow path for an engine with BPR = 14.

Basic Aerodynamic Analysis and Efficiency Correlation

Based on the geometrical model and thermodynamic cycle data, a basic aerodynamic analysis is conducted to estimate velocity triangles and the corresponding stage flow and loading coefficients. Then polytropic design efficiencies of turbo components at cruise operation are estimated by means of a correlation approach [24] and are updated in the thermodynamic cycle model.

- The fan efficiency is modelled as a function of the fan pressure ratio and the fan face Mach number.
- For turbomachinery of the core engine, Smith charts are used to obtain a baseline efficiency in dependence on inlet-outlet-averaged flow and loading coefficients. The applied compressor loss model accounts for the effect of inlet Mach number.
- Varying inlet conditions are addressed by a correction based on the Reynolds number index.
- The effect of component size is considered by adding a correction term according to the corrected inlet mass flow.
- For turbines, the reduction of efficiency due to cooling air is taken into account.
- To account for technological component maturity, an efficiency delta based on the entry into service is added.

Mass Estimation

The dry bare engine mass is modelled on the level of parts with respect to the flow path geometry, thermodynamic cycle data, selected material and spool speeds. Individual masses are estimated for blades, disks, connecting devices, casings, shafts, frames and ducts as well as for the gearbox. The procedure is presented by Häßy et al. [23] and follows the approach of Pera et al. [30] and Klees et al. [31]. Compared to [23], re-calibrated correlations for disks and frames are applied, a model for the mass of variable inlet guide vanes (VGVs) is introduced, double casing structures are accounted for and the shaft mass is calculated according to Bretscheider [32]. The nacelle, pylon, nozzles, thrust reverser, anti-icing system and fuel supply to the engine interface are considered to be aircraft components and are modelled with the tool openAD (cf. III.C). A representative mass breakdown of the engine for BPR = 14 is presented in table 2.

- A composite casing and liner assembly is assumed for the fan. A light weight casing enables the implementation of higher bypass ratios and larger fan diameters since additional mass is limited due to the low density of composite materials.
- Also for the fan rotor and bypass stator blades composite materials are assumed. Aluminium is used for the fan stator blades in the core section.
- Titanium is assumed for the booster. The high-pressure compressor stages with a maximum inlet temperature below 680 K are made of Titanium and above this threshold Nickel-base alloy is used.
- The first four stages of the high-pressure compressor are equipped with variable inlet guide vanes and corresponding devices for pitch control.
- Nickel-base alloy is assumed for the high- and low-pressure turbine. For the last stages of the low-pressure turbine, titanium aluminide alloy is used when the maximum operating temperature is less than 1000 K.
- The high-pressure compressor and turbine are modelled with a double casing structure.

Emission Prediction

The emission index (EI) relates the emitted amount of a species to the amount of fuel burned. The emission index of carbon dioxide (CO2) and water (H2O) only depends on the composition of the fuel. The emission indicies for nitrogen oxides (NOx) and non-volatile particulate matter (nvPM) respectively soot depend not only on the fuel properties but also on the temperature and pressure during operation of the engine. In order to model EINOx and EInvPM, a

Table 2 Mass breakdown on component level and share of different parts for BPR = 14.

Component	Total [kg]	Share [%]	Rotor [%]	Stator [%]	Disk [%]	Connecting [%]	Casing [%]	Sealing [%]	VGV [%]	Inlet Cone [%]
Fan	1219	18.1	17.8	15.1	8.1	0.0	58.1			0.9
Fan Frame and ICD 1	255	3.8								
Booster	384	5.7	9.2	29.0	24.9	6.5	30.5	0.0	0.0	
Intermediate Frame and ICD 2	141	2.1								
HPC	535	7.9	5.4	8.6	23.5	4.8	43.4	2.6	11.7	
Combustor	95	1.4								
HPT	297	4.4	6.1	7.8	37.4	2.0	38.4	8.4	0.0	
ITD	17	0.3								
LPT IGV Frame	34	0.5								
LPT	903	13.4	10.5	24.5	26.3	3.7	26.6	8.4	0.0	
TEC Duct and Frame	121	1.8								
HP Shaft	28	0.4								
LP Shaft	307	4.5								
Gearbox	738	11.0								
Accessories	765	11.4								
Not Modelled	902	13.4								
Bare Engine	6742	100.0								

reference combustor characteristic is employed that was calibrated using certification data from the ICAO aircraft engine emissions database [26]. The combustor Talon X Block-D of the PW1100G-JM [33], which features a rich-burn quick-quench lean-burn (RQL) combustor concept, is selected to calibrate the emission model. For this study, a constant RQL-combustor technology is assumed and no redesign of the combustor is considered.

- Kerosene Jet A-1 with a fuel heating value of 43.25 MJ/kg is assumed. The corresponding emission indicies are EIH2O = 1239 g/kg for water and EICO2 = 3156 g/kg for carbon dioxide.
- The p_3-T_3-method is applied for the prediction of EINOx [34]. The available emission data for calibration is extrapolated on a physical basis using the method presented by Stöpler [35] to obtain a reference function that covers a larger temperature range in terms of T_3.
- The method according to Döpelheuer [36] is applied to model EInvPM (soot) in terms of total particle mass. The particle number is then modelled as a function of particle mass and diameter. The particle diameter is correlated with T_3.

C. Aircraft Design Process

A long-haul, wide-body aircraft is chosen as reference. The so-called D300-XRF1 reference aircraft designed by DLR [37] enables a differentiated evaluation of new technologies by providing a high degree of consistency within the aircraft design. The D300-XRF1 is designed for 300 passengers with a 3-class cabin layout resulting in a fuselage with a length of 63.9 m. The ICAO aerodrome category E applies to the D300-XRF1 aircraft with a wingspan of 58 m and an aspect ratio of 8.98 (cf. Fig. 5).

By forecasting evolutionary technological improvements for the expected market maturity EIS = 2035, the reference aircraft is improved. It is assumed that mass reductions of 15 % in the wing structure, 10 % in the fuselage structure, and 20 % in the empennage structure are achievable due to advances in manufacturing and assembly methods as well as due to the extended use of composite materials. Additionally, an improvement of the aerodynamic performance by additional winglets and further optimization of airfoils is assumed resulting in an average lift-to-drag ratio (LoD) close to 20 at cruise operation.

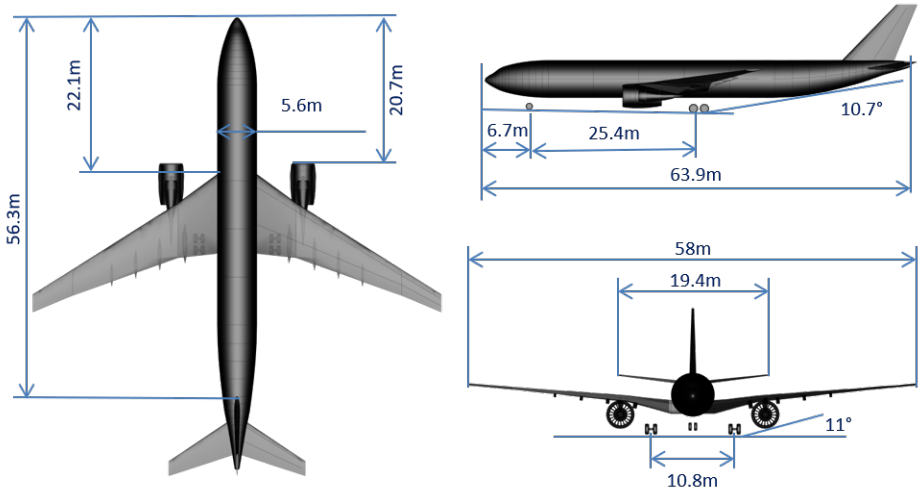

Fig. 5 Geometry of the reference aircraft D300-XRF1 [37].

The top-level aircraft requirements (TLARs) for the considered future aircraft are listed in Table 3. Two flight missions with different range are analyzed: The design mission with a range of 5500 NM and a payload of 31.5 t consisting of 300 passengers with 105 kg each. The typical mission is the most flown mission according to [38] and has a range of 4000 NM with a payload of 31.8 t. Both missions are flown with a Mach number of 0.83 at cruise. The required initial cruise altitude for the design mission is specified with flight level (FL) 330. For the typical mission, the most efficient initial cruise altitude is selected considering allowed flight levels.

Table 3 Top-Level Aircraft Requirements (TLARs)

Parameter	Unit	Value
Technology Status	Year	2035
Design Mission Range	NM	5500
Typical Mission Range	NM	4000
Design Cruise Mach Number	-	0.83
Service Ceiling	ft	43000
Number of Passengers (3 Class Standard Layout)	-	300
Design Mission Payload (105 kg/PAX)	t	31.5
Typical Mission Payload	t	31.8

The OAD process (cf. Fig. 6) is set up in the workflow-driven integration platform RCE (Remote Component Environment) [39], which provides a framework for collaborative integration and combination of multiple tools. Within this multidisciplinary design analysis and optimization (MDAO) process, the various sub-processes communicate with each other via their inputs and outputs in the common language known as the "Common Parametric Aircraft Configuration Schema" (CPACS) [40, 41]. CPACS provides a data definition for the overall aircraft characteristics, i.e. geometry, aerodynamics, propulsion, masses and performance, and supports the exchange of information between the individual sub-processes. In the following, the OAD process used in this publication is briefly described and for more details it is referred to Fröhler et al. [37].

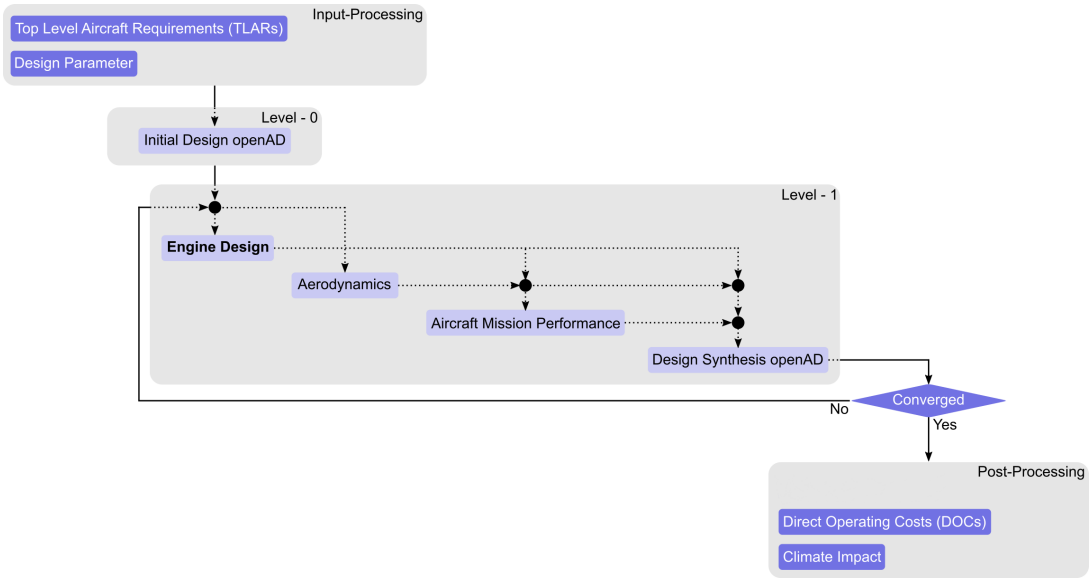

Fig. 6 Conceptual overall aircraft design process.

To initialize the OAD process, the level-0 conceptual design tool openAD [42] is used, which produces an initial geometry definition and an initial performance estimate of the aircraft based on the TLARs and design parameters. Subsequently, level-1 disciplinary tools with higher fidelity are used to refine the initial openAD results. In the engine design subprocess, the rubber engine model is integrated and provides the engine performance. In parallel, DLR's in-house tool Lifting-Line [43] is used to calculate the aerodynamic polars for the entire flight envelope, which is based on potential flow theory. In addition, handbook methods are used to approximate the viscous drag using (semi-)empirical methods [44, 45]. The empennage is calibrated and sized based on the volume coefficient of the reference aircraft, which is calculated using the empennage reference area and lever arm. While the size of the empennage is influenced by the thrust and diameter of the engine, the expected changes are relatively small and the volume coefficient for the VTPs is kept constant. The engine and aerodynamic performances are then transferred to the mission calculation of the aircraft, which estimates the high-speed mission performance and energy consumption of a selected payload-range combination [42]. For each block mission, an additional reserve mission with a range of 200 NM is calculated and contingency fuel of 5 % is added. As a final step, the higher fidelity results are fed back into openAD as a synthesis to obtain a consistent aircraft design. The post-processing in the context of this publication includes an assessment of the climate impact according to [46] and an evaluation of the direct operating costs (DOC) according to [47].

D. Approach for Rubber Engine Integration

Model Creation

The covered design space for the demonstration case is spanned by two thrust requirements and the BPR at mid cruise. The first thrust is specified for TOC conditions. The second thrust is given by the thrust ratio relating MTO-SLS to TOC operation. The individual parameter ranges are given in Tab. 4. Specifying one absolute thrust and ratios for other operating conditions has the advantage that all thrusts are automatically scaled when the total system size changes. Thereby, unrealistic thrust combinations that will never be requested are avoided. The thrust at TOC and MTO are the most relevant for engine sizing and affect the selection of the thermodynamic cycle since different technological limits are hit at each condition. The thrust for the remaining operating conditions cruise, EOF and 2ndSeg are established by assuming constant thrust ratios with respect to TOC respectively MTO-SLS.

For the creation of the hybrid surrogate-based rubber engine model, the conceptual engine design workflow (cf. Sec. III.B) is used to generate the required training data. The parameter space is populated with engine designs using a full-factorial sampling strategy with 5 equally distributed samples per dimension and 125 samples in total. For surrogate modelling, the toolbox 'Surrogate Modeling for AeRo Data Toolbox in python' (SMARTy) [48–50] is used. A cubic radial-basis-function kernel with quadratic trend functions and without regression is selected to create the surrogates for the rubber engine model.

Table 4 Parameter space covered by the rubber engine model.

Parameter	Unit	Min.	Max.
Thrust at TOC	[kN]	50.0	70.0
Thrust Ratio MTO-SLS to TOC	[-]	4.5	6.0
BPR at cruise	[-]	8.0	18.0

For each combination of model inputs, the surrogates output all relevant parameters that uniquely define the corresponding engine design. To define the thermodynamic cycle of a specific engine, a consistent parameter set is provided comprising the engine mass flow, fan inlet Mach number, compressor pressure ratios, fuel-to-air-ratio, relative cooling air demand, spool speeds, gear ratio, pressure loss in the bypass duct and turbomachinery efficiencies. Other parameters of the engine performance model are not varied within the thermodynamic cycle design and remain constant. In order to restrict the operational range of each engine, also limiting values for engine parameters are output of the surrogates, e.g. rotational shaft speed, temperatures, pressures. Further outputs are the total dry engine mass, center of gravity and fan tip radius, as well as the maximum radius, wetted area and length of the nacelle.

Calculation of Engine Performance Maps

After specifying input parameters for the rubber engine model, the internal surrogates are evaluated and the tool for performance analysis is initialized according to the selected engine design. Then engine performance maps are calculated and provided for the overall aircraft design process. For the map calculation, a flight envelope is defined (cf. Fig. 7a) by maximum ceiling altitudes for low- and high-speed operation, a maximum flight Mach number and bounds for the calibrated air speed to represent the structural and stall limits of the aircraft. The operating range inside the flight envelope is discretized by specifying mandatory altitudes and mach numbers in combination with maximum allowed step sizes. Mandatory values comprise typical flight levels and Mach numbers to minimize interpolation errors when the map is applied. Therefore, the discretisation points are not necessarily distributed equally in the flight envelope (cf. Fig. 7a). For each discrete combination of Mach number and altitude, an operating line is calculated by varying the engine power. The operating line is restricted by the idle rating at low and by a maximum rating at high power. The idle rating is defined by minimum required values for the relative corrected fan speed and the pressure ratio of the core nozzle. To limit the power to the top, the MCL rating for unlimited use and the MTO rating, which is time limited to 5 min, are considered. For both, maximum values for the relative corrected fan speed, absolute rotational speed of the low-pressure shaft and the stator outlet temperature T_{41} are set according to the output of surrogate models.

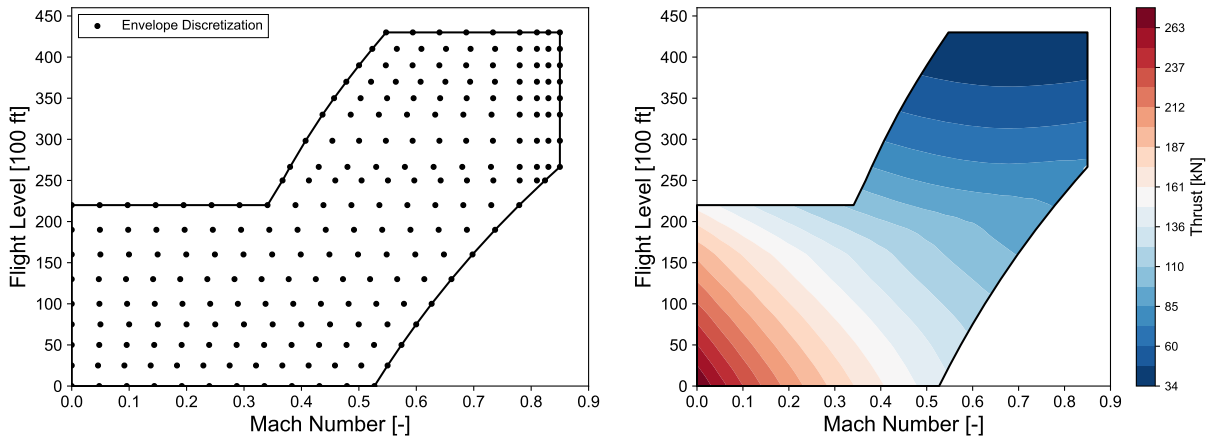

(a) Discretisation of flight envelope

(b) Engine thrust at MCL rating

Fig. 7 Engine performance map calculated with the rubber engine model for BPR = 14.

Exemplary, the maximum available thrust for the MCL rating is shown in figure 7b for BPR = 14. For the MTO rating, the thrust is flat rated with a kink point at a deviation from the outer air temperature (ΔT_{ISA}) of 15 K. Two maps are calculated: The first map contains the operating range between idle and MTO for the low speed envelope. The second map provides the range between idle and MCL for the full flight envelope. In total, 15000 engine operating points are calculated in less than 6 min on a modern personal computer using one core. The rubber engine model does not slow down the used OAD workflow since another tool running in parallel requires more time for execution. By changing the performance map resolution, the execution time of the rubber engine model can be adapted to the individual needs of an OAD process.

Convergence Strategy

The overall aircraft design workflow implements a fixed point iteration approach in order to achieve convergence of involved disciplines and tools on level 1 (cf. Fig. 6). The engine selection and performance map calculation is executed in parallel to the aerodynamic analysis and subsequently the flight mission is calculated. The results of disciplinary tools are fed back into the aircraft model and the convergence status is checked by comparing new values with previous ones. The convergence criteria is that the changes in maximum take-off mass (MTOM), operating empty mass (OEM), lift coefficient and drag coefficient at mid cruise are below a threshold of $\epsilon < 10^{-4}$. With respect to the engine model, the history of requested thrusts at TOC is tracked. A thrust damping is activated when the relative change in thrust at TOC exceeds 2 %. Then the new thrust value is calculated with a = 0.4 according to equation 1.

$$x^{*}_{new} = x_{new}\left(\frac{x_{previous}}{x_{new}}\right)^{a} \tag{1}$$

When the required initial flight level FL330 is not reached for the design mission due to a lack of thrust, the new thrust value is increased by applying a growth factor of 1.05. An exemplary residual plot is shown in figure 8. Convergence is usually reached after 5 to 10 iterations depending on the start values. One iteration requires ≈ 12 min and therefore, each aircraft configuration converges after one to two hours of execution.

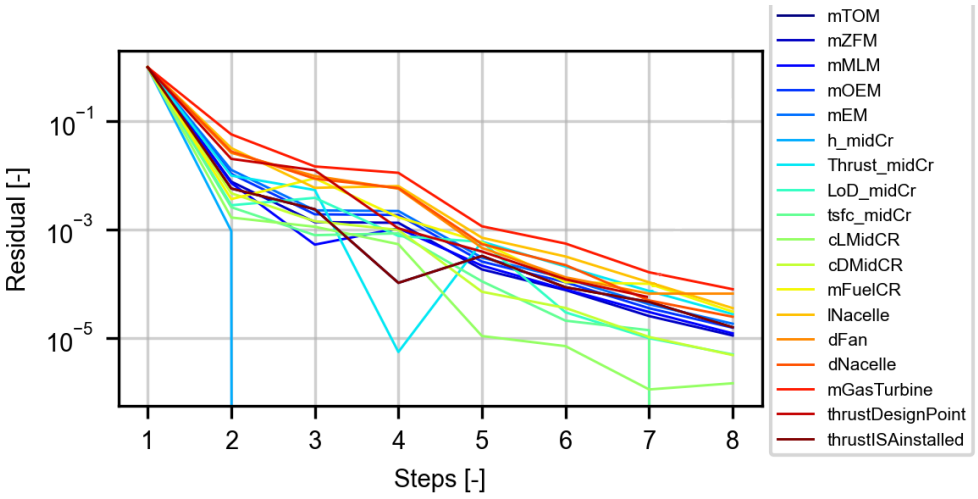

Fig. 8 Exemplary residual plot showing the convergence history.

IV. Results and Discussion

In order to demonstrate the hybrid surrogate-based rubber engine model approach, an overall aircraft design study with focus on the propulsion system is performed. The demonstration case aims at identifying the optimal BPR in terms of mission fuel burn considering snow ball effects. In particular, the conflict between size and mass of a geared turbofan engine on the one hand and the selection of the BPR for increased efficiency on the other hand is addressed for a long-haul wide-body aircraft with entry into service in 2035. In addition, it is presented how the selection of the BPR affects NOx and nvPM emissions, climate impact and DOC. The results of the OAD workflow with an integrated rubber

engine model are presented in the following sections and the key driving interactions between the airframe and engine are discussed. For the typical mission, the flight altitude and Mach number are shown for three different bypass ratios at mid cruise in figure 9. For all bypass ratios, the best initial cruise altitude is FL 330 and two step climbs are made in the course of the mission. The ground distance where the step climb takes place increases with the bypass ratio. The respective payload range diagrams are depicted in figure 10 with marked design and typical missions.

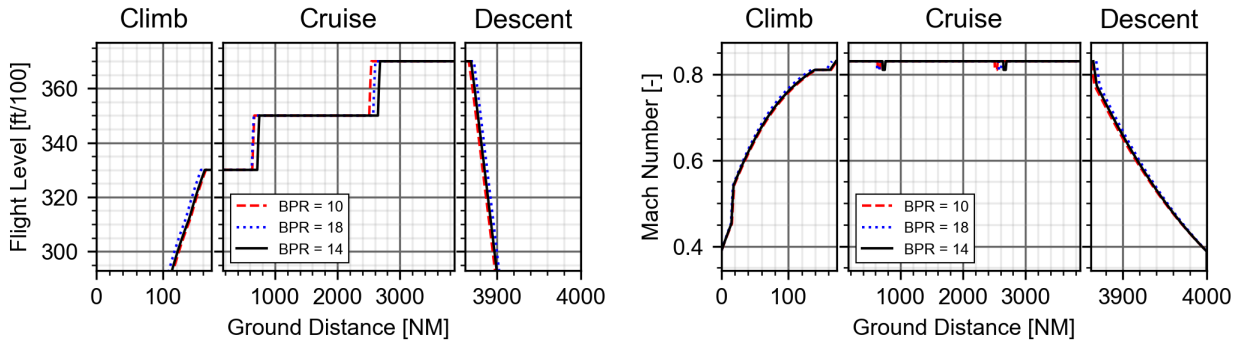

(a) Flight level

(b) Mach number

Fig. 9 Flight altitude and Mach number for different design bypass ratios at cruise for the typical mission.

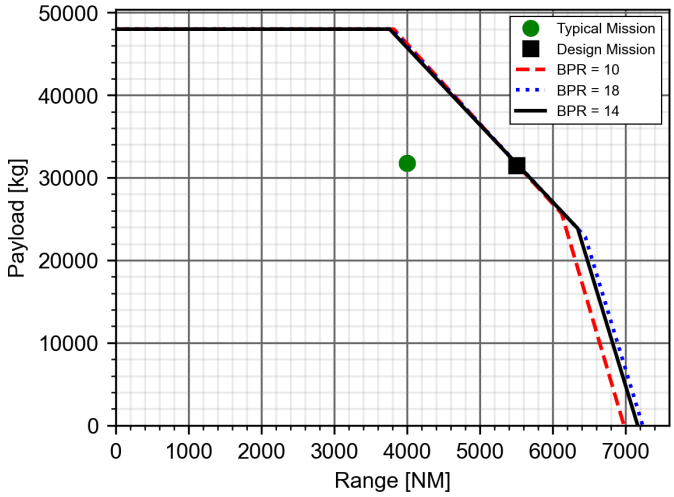

Fig. 10 Payload range diagram for different bypass ratios.

A. Overall Aircraft Parameters

The resulting trends of overall aircraft parameters for a variation of BPR at mid cruise are shown in figure 11. All parameter variations are presented relative to the configuration with BPR = 14.3. The maximum take-off mass, engine and aircraft efficiency and the resulting block fuel for the typical flight mission are shown in figure 11a. The thrust specific fuel consumption (TSFC) of the engine and the lift-to-drag ratio (LoD) of the aircraft are averaged for the cruise segment. With an increasing BPR, the engine accelerates a larger mass flow at a lower fan pressure ratio leading to smaller nozzle velocities. The smaller difference between flight and jet velocities results in an improved propulsive efficiency and thrust specific fuel consumption (TSFC). This positive effect is observable especially for small BPRs and declines degressively (cf. Fig. 11a). The TSFC for the flight trajectories is shown in figure 12a. A reduction of 4 % in TSFC is achieved for the average cruise segment increasing BPR from $\approx$ 10 to 14 whereas the further increase to BPR $\approx$ 18 has a small effect with less than 1 %.

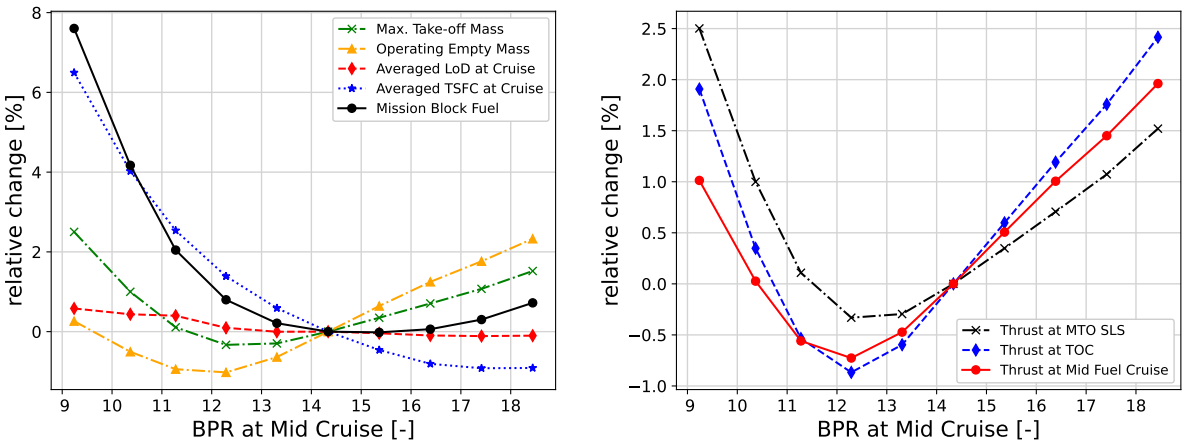

(a) Overall aircraft parameters

(b) Engine thrust

Fig. 11 Variation of overall aircraft parameters and thrust with the design bypass ratio at cruise.

The overall aircraft lift-to-drag-ratio (LoD) averaged for the cruise segment slightly decreases for larger BPRs since a larger wetted area of the nacelle leads to more drag counts (cf. Fig. 11a). The trend of LoD along the typical mission is presented in figure 12b. For a constant flight level at cruise, the aircraft burns fuel and loses mass resulting in less required lift, smaller angles of attack and a decrease in LoD. At a certain point, a step climb to a more efficient cruise altitude is made. Compared to this effect, the impact of BPR on aerodynamic efficiency respectively LoD is small.

The maximum take-off mass (MTOM) and the required thrusts (cf. Fig. 11b) reach a minimum for BPR $\approx$ 12. For lower BPRs, the trends in MTOM and thrust demand are dominated by the required fuel mass that changes significantly due to the strong gradient in TSFC. For higher BPRs, the growing engine size adds additional mass and required lift as well as parasitic drag whereas the benefit in TSFC levels out. As a result, the operating empty mass (OEM) changes less than MTOM for BPR < 12 and vice versa for BPR > 12. However, the maximum variation in thrust is small with less than 3.5 % for the investigated range of BPRs. The course of thrust for the typical mission is visualized in figure 12c.

The minimum mission block fuel for the typical mission occurs at BPR = 14-15. From there, a further reduction in TSFC with BPR is outweighed by additional mass and drag leading to more block fuel. For high bypass ratios with BPR > 15-16, a variable fan or nozzle is required to maintain a sufficient surge margin during low speed operation, e.g. take-off. The additional hardware would also add mass which is not accounted for here. Hence, the increase in fuel burn for BPR > 15 is expected to be more significant than observed here. The overall aircraft mass as a function of ground distance is shown in figure 12d for the typical mission. The change in aircraft mass corresponds to the amount of fuel burned. The trajectory for BPR = 14 has the lowest aircraft mass at take-off to accomplish the flight mission since the engine was selected for optimal block fuel. However, the landing mass is almost the same as for BPR = 10 since the OEMs differ by only $\approx$ 0.5 %. The course for BPR = 18 is offset compared to BPR = 14 since the OEM is $\approx$ 2 % higher and almost the same amount of fuel is burned during the mission.

The selected BPR also impacts the payload range diagram as shown in figure 10. Since all aircraft are designed for the same design mission, the payload range characteristic do not alter much with BPR. Only on the lower right side of the payload range diagram (payload < 24 t), the maximum range for a given payload increases continuously for a growing bypass ratio. In this region of operation, the tank is completely filled with fuel at take-off and therefore, the sensitivity with respect to TSFC is higher compared to the design or typical mission. As a result, the maximum achievable range occurs for BPR = 18, even if BPR = 14 is superior for the design and typical mission. However, the lower right region in the payload range diagram is of minor importance for usual operation.

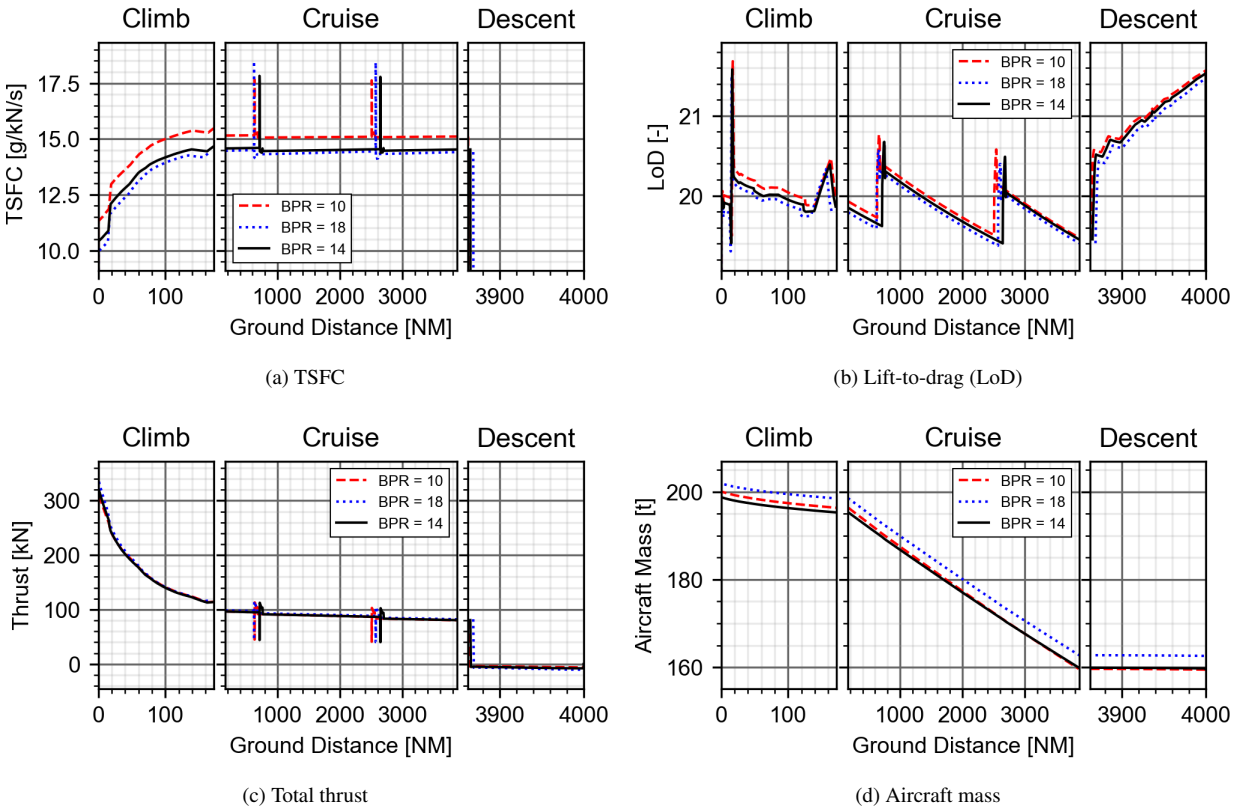

(a) TSFC

(b) Lift-to-drag (LoD)

(c) Total thrust

(d) Aircraft mass

Fig. 12 Overall aircraft parameters for different bypass ratios at cruise for the typical mission.

B. Dimensions and Mass

The relative change of engine related dimensions and mass with BPR is shown in figure 13a. Engine flow paths for BPR = 10, 14 and 18 are compared in figure 14 to discuss geometrical changes.

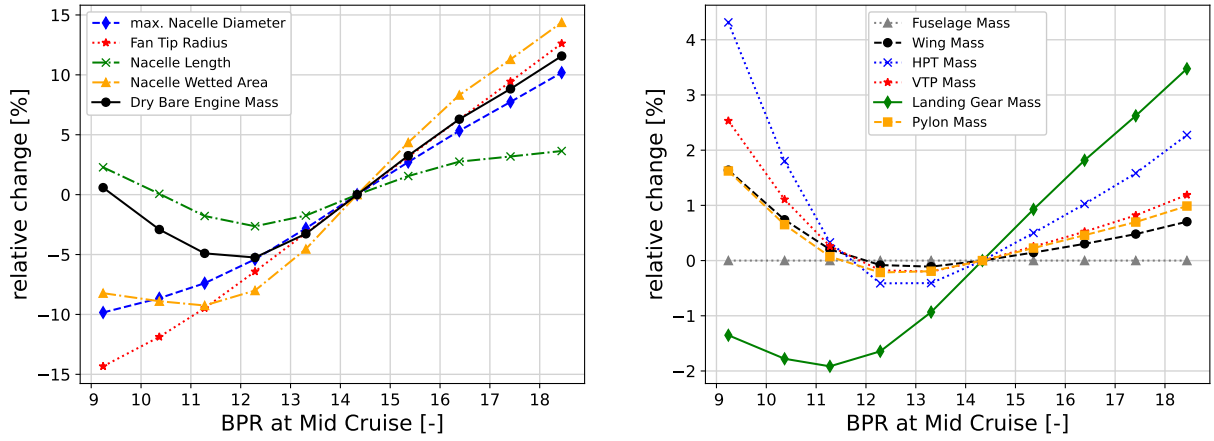

(a) Engine dimensions and mass

(b) Aircraft component mass

Fig. 13 Variation of dimensions and mass with the bypass ratio at cruise.

The engine mass flow increases with BPR while the maximum flow capacity is kept constant. As a result, the fan tip radius grows with BPR. The length of the nacelle is modelled in dependence on the engine length (cf. Sec. III.B) and has a minimum at BPR ≈ 12.The engine length is affected by several aspects: First, the axial length of turbo components change differently for a variation of BPR. Constant blade aspect ratios are maintained for all blades. Hence, the length of a component depends on its blade height. The fan blade height and therefore, the axial length of the fan increase with BPR (cf. Fig. 14). For a constant Mach number, the blade height at the booster inlet depends on the mass flow rate and the fan pressure ratio. For a higher BPR, the fan pressure ratio and mass flow decrease but the blade height at the booster inlet increase. Second, additional stages for the booster and high-pressure compressor are required at lower BPRs to keep the aerodynamic loading below the assumed limits (cf. Fig. 14). This leads to a longer engine for BPR = 10 compared to BPR = 14 even if the fan is larger for the latter one. The maximum nacelle diameter grows continuously with BPR since it mainly depends on the fan tip radius. The nacelle thickness is scaled with nacelle length whereby the trend of an increasing nacelle diameter with BPR is mitigated for lower BPRs. The trend of the dry bare engine mass is mainly driven by the fan and gear box mass. From BPR = 9 to 18, the related mass increases almost by a factor of 2. For BPR < 12, the increase in engine mass is related to slightly larger cores with additional stages for the booster and high-pressure compressor.

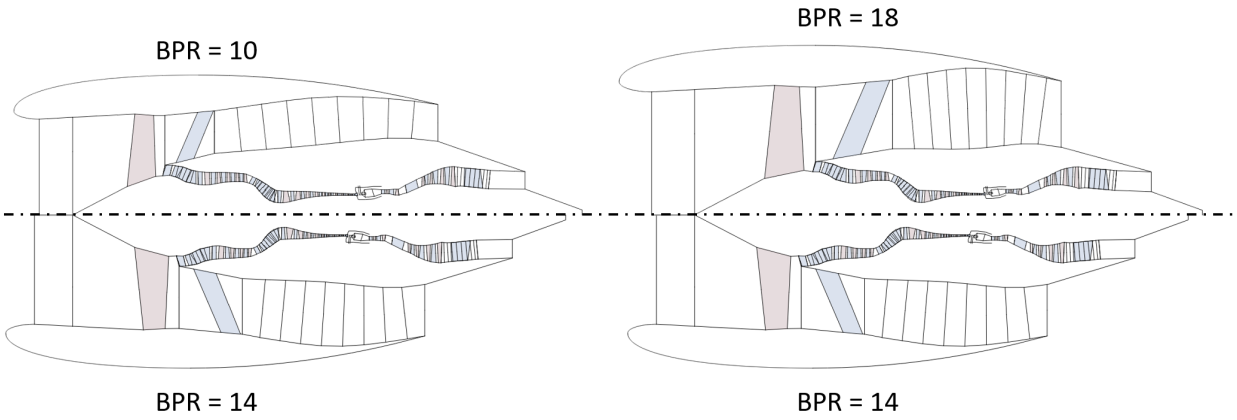

Fig. 14 Comparison of engine geometry for the bypass ratios 10, 14 and 18.

The relative change in the mass of airframe components is shown in figure 13b. The fuselage mass and geometry remains the same for the presented study since the same number of passengers and payload is transported. The mass of the wings, horizontal and vertical tail planes and the pylons follow the trend of required thrust and MTOM. For Example, when a mass increment is added to the aircraft, more lift and wing area are required leading to more drag and required thrust. As a result, all components grow in size and mass until lift, drag and thrust are balanced. The mass of the landing gear depends on its length and the aircraft's landing mass. The required length of the landing gear increases with BPR to ensure a sufficient ground distance of the nacelle (cf. Fig. 15). The OEM which indicates the trend of the landing mass reaches its minimum at BPR ≈ 12. In total, both effects lead to a minimum landing gear mass at BPR ≈ 11.

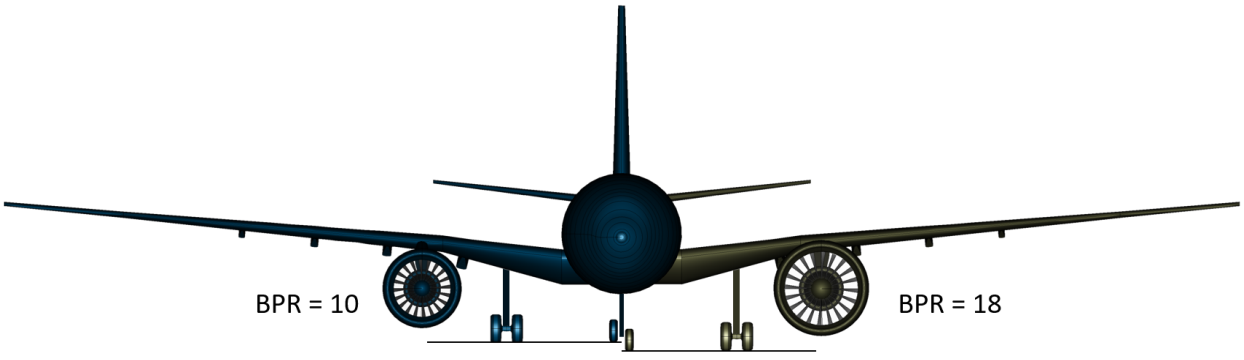

Fig. 15 Comparison of aircraft geometry for BPR = 10 and 18.

C. Emissions

The emission assessment for CO2 and H2O is straight forward since complete combustion can be assumed and the emissions are directly proportional to the fuel flow. However, the prediction of NOx and nvPM (soot) emissions during conceptual design is more uncertain. The forecast of future combustion technology is even more challenging since NOx and nvPM emissions are related in a strongly non-linear manner with the concrete geometry of the combustor, the flow field and the mixing of air and fuel. Here, a correlation-based approach is used that was calibrated using a fixed characteristic of a RQL-combustor. Differences have to be expected for other combustor types, e.g. lean-burn. No redesign or technological improvement is assumed. Therefore, the presented trends for NOx and nvPM aim at giving an insight into the general physical interrelations and do not claim to represent exact values.

For a RQL combustor, there are three typical zones: First, the combustion is fuel-rich to ensure operational stability. Due to the excess of air the combustion temperature and NOx production are limited. Second, air is rapidly added and mixed with the combusting gas in the quenching zone to quickly make the transition to fuel-lean conditions. In the mixing zone, regions with or close to the stoichiometric ratio are not avoidable. There, high NOx production rates occur due to high local temperatures. In the third zone, the combustion is fuel-lean and the NOx production rate is small. The FAR exponent of the p3-T3-method [34] is typically set to zero for a RQL concept since the quenching zone is dominating NOx production and cannot be avoided with a change in the global FAR of the combustor.

The production of NOx and nvPM emissions is directly connected to the thermodynamic parameters at the combustion chamber. The relative change in average cruise values for the inlet temperature T_3, fuel to air ratio (FAR), the combustor outlet temperature T_4 and the overall pressure ratio (OPR) are shown for the typical mission in figure 16a. The inlet pressure level is indicated by OPR since ambient conditions are the same for all shown data points.

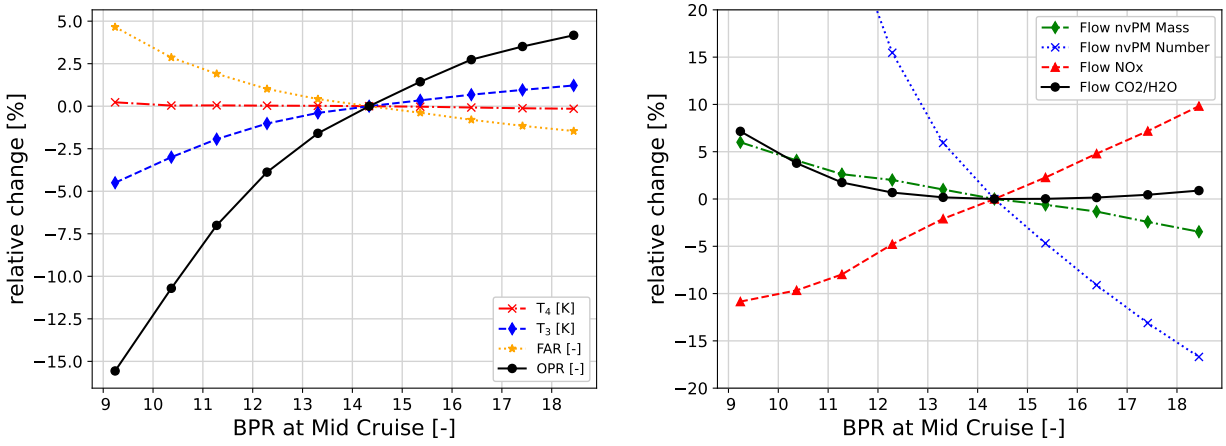

(a) Engine thermodynamic parameters

(b) Total flow of emissions

Fig. 16 Trend of thermodynamic parameters and emissions for a RQL-combustor concept with the design bypass ratio at cruise.

The combustor outlet temperature T_4 does barely change with BPR since all engines are designed for the same T_{41} at TOC, which is relatively close to cruise conditions. In contrast, the thrust lapse effect grows with the BPR, i.e. the loss in thrust from sea level to cruise operation for a similar operating state of the engine becomes larger. Therefore, with increasing BPR, the engine has to be operated at a higher relative load at cruise conditions to provide the required thrust. Since a low speed operating point during take-off is sizing for OPR with $T_{3,max}$ = 1000 K, the inlet pressure and temperature of the combustor at cruise significantly increase with BPR. The fuel-to-air ratio FAR decreases since less fuel has to be added in relation to the air mass flow to reach the almost constant T_4.

The average emissions at the cruise segment are shown in figure 16b. The emission of CO2 and H20 follow the fuel flow and reach a minimum between BPR = 14-15. Nitrogen oxide emissions increase significantly with BPR since higher levels of combustor inlet pressure and temperature are present for cruise operation driven by the thermodynamic cycle. In the case of a lean-burn combustor, it can be expected that NOx emissions decline when FAR is reduced. However, an elevated level of inlet temperature and pressure would also lead to more NOx for lean-burn combustion.

Therefore, the presented trends in NOx are only valid for a RQL combustor. The mass and number of emitted nvPM reduce with increasing BPR since higher temperature and pressure as well as a smaller FAR lead to higher decay rates at cruise.

D. Climate Impact

In order to assess how the selection of BPR affects climate impact, the average temperature response (ATR) is calculated according to [46] for each aircraft configuration considering a time period of 100 years. Individual values of ATR for CO2, NOx, H2O, soot and aircraft induced cloudiness (AIC) are estimated. The change of ATR with the engine's BPR is shown in figure 17a. The magnitude of single effects with respect to the total ATR is presented in figure 17b for BPR = 14. The climate impact of CO2 and H2O shows the same trend as the fuel flow. The effect of soot also follows this trend since the tool for ATR calculation could not process the predicted nvPM emissions and a constant emission index was assumed. However, the direct effect of soot emissions is neglectable (cf. Fig. 17b). The cooling and warming effect of NOx emissions increase both with BPR. The warming effect of NOx emissions outweighs the cooling effect resulting in a positive ATR in total. Therefore, the climate impact caused by NOx increase with BPR. The change of ATR related to AIC almost remains the same since all aircraft are operated at the same flight levels during the typical mission. Aircraft induced cloudiness will be affected by the number of emitted soot particles since these serve as nuclei during condensation processes. Hence, less emitted particles reduce the chance of contrail formation. This effect is not accounted for here. In total, the minimum ATR is reached for BPRs between 11 and 12. Please note, the presented climate impact in terms of ATR is subject to uncertainty since a prediction approach is used that introduces simplifications in order be applicable for conceptual design.

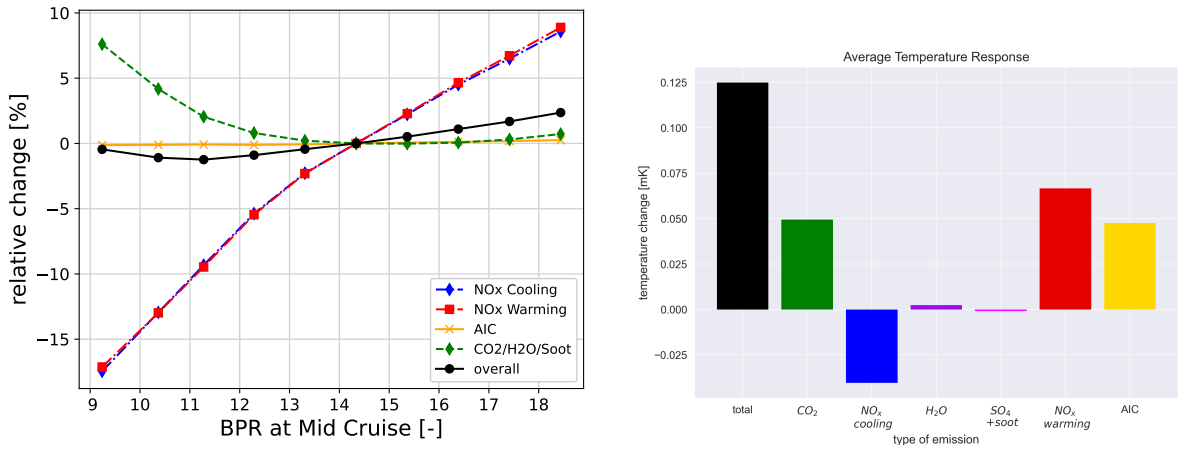

(a) Average temperature response (ATR)

(b) ATR contribution for BPR = 14

Fig. 17 Relative change of climate impact in terms of ATR with the bypass ratio for the typical mission.

E. Direct Operating Costs

The direct operating costs (DOC) comprise fees as well as maintenance, crew, capital and fuel costs. The relative change in DOC with the selected engine BPR is depicted in figure 18a for the typical mission. The share of different cost categories is shown for BPR = 14 in figure 18b. Costs for capital, energy and fees make up the largest portions. For variations of BPR, the energy costs follow the trend of block fuel. The costs for crew remain almost unchanged since the same mission is flown at a constant Mach number and flight time do barely change. The other cost categories follow the MTOM. In total, minimum DOC is reached for BPR = 12-13. However, the prediction of costs is uncertain and rather indicates a rough trend.

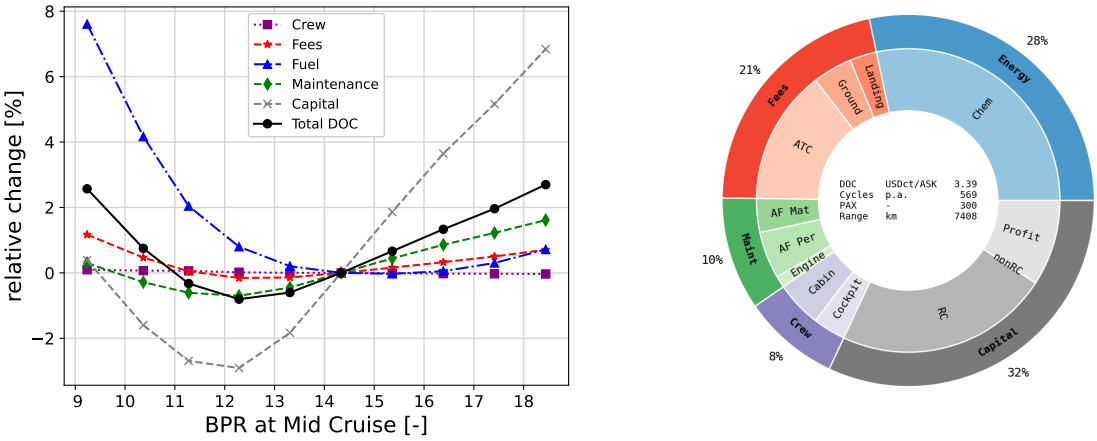

(a) Trend of costs

(b) Cost categories (BPR = 14)

Fig. 18 Impact of the engine BPR on direct operating costs (DOC) for the typical mission.

V. Conclusion

The concept of a hybrid surrogate-based rubber engine model is demonstrated for a long-haul tube-and-wing aircraft configuration with entry into service in 2035. The rubber engine concept uses surrogate-models to store design information for a range of different engine designs. When a concrete engine is selected, an embedded tool for thermodynamic analysis is initialized corresponding to the surrogate outputs and engine performance as well as emissions are calculated on-demand. For the demonstration case, a generic rubber engine model for a geared turbofan architecture is integrated into a conceptual workflow for overall aircraft design. The rubberized model enables the selection of different engine designs in terms of bypass ratio and required thrust at top of climb and maximum take-off. To generate training data for the surrogate models, a conceptual engine design process is applied that comprises thermodynamic cycle calculation, flow path sizing, simplified aerodynamic analysis, correlation-based efficiency prediction, engine mass estimation and emission calculation.

With the rubber engine model integrated into the aircraft design workflow, a bypass ratio study on overall system level is conducted to investigate the resulting trends in block fuel, emissions, climate impact and direct operating costs. For an increasing bypass ratio, engine efficiency is improved but nacelle diameter and engine mass grow and counteract the fuel benefit. Here, a bypass ratio of 14 to 15 is found for optimal block fuel considering the most flown mission. The minimum in maximum take-off mass is located at lower bypass ratios between 12 and 13. Carbon dioxide and water emissions follow the trend of block fuel. However, nitrogen oxide emissions significantly increase with the selected bypass ratio for an assumed RQL combustor. For a similar operating state of the engine, the available thrust decreases with flight altitude. This thrust lapse effect is more distinct for higher bypass ratios. Since the sizing operating condition for the overall pressure ratio is during take-off, the combustor's inlet pressure and temperature at cruise increase with BPR in order to provide the required thrust. This leads to more NOx emissions at cruise predicted with the RQL combustor model. In contrast, the emission of non-volatile particulate matter at cruise is reduced since higher load favors the decay rate of particles. In terms of climate impact, the average temperature response has a minimum close to a bypass ratio of 11. For higher bypass ratios, CO2 and H2O emissions can be further reduced but increasing NOx emissions counteract the positive effect on climate. A bypass ratio close to 12 is optimal with respect to direct operating costs since the impact of maximum take-off mass on costs outweighs fuel savings for higher bypass ratios.

In the future, the hybrid surrogate-based rubber engine approach will be used to provide different engine designs and the corresponding operating characteristics for various projects within DLR. This enables collaborative and multidisciplinary research by an efficient exchange of disciplinary knowledge. In addition, the herein presented study will be extended to investigate the impact of overall pressure ratio and turbine inlet temperature on the aircraft's key performance indicators. Additionally, the trend of NOx emissions with the engine's bypass ratio will be compared for different combustor types.

References

[1] Vera-Morales, M., and Hall, C. A., "Modeling Performance and Emissions from Aircraft in the Aviation Integrated Modelling Project," *Journal of Aircraft*, Vol. 47, No. 3, 2010, pp. 812–819. https://doi.org/10.2514/1.44020.

[2] McDonald, R. A., "Mission Performance Considered as Point Performance in Aircraft Design," *Journal of Aircraft*, Vol. 48, No. 5, 2011, pp. 1576–1587. https://doi.org/10.2514/1.C031290.

[3] Gur, O., Bhatia, M., Mason, W. H., Schetz, J. A., Kapania, R. K., and Nam, T., "Development of a framework for truss-braced wing conceptual MDO," *Structural and Multidisciplinary Optimization*, Vol. 44, No. 2, 2011, pp. 277–298. https://doi.org/10.1007/s00158-010-0612-9.

[4] Neufeld, D., Chung, J., and Behdinian, K., "Aircraft Conceptual Design Optimization Considering Fidelity Uncertainties," *Journal of Aircraft*, Vol. 48, No. 5, 2011, pp. 1602–1612. https://doi.org/10.2514/1.C031312.

[5] Risse, K., and Stumpf, E., "Conceptual aircraft design with hybrid laminar flow control," *CEAS Aeronautical Journal*, Vol. 5, No. 3, 2014, pp. 333–343. https://doi.org/10.1007/s13272-014-0111-6.

[6] Risse, K., *Preliminary overall aircraft design with hybrid laminar flow control: Vorentwurf von Flugzeugen mit hybrider laminarer Strömungskontrolle*, Berichte aus der Luft- und Raumfahrttechnik, Shaker Verlag, Aachen, 2016.

[7] Antcliff, K. R., Guynn, M. D., Marien, T., Wells, D. P., Schneider, S. J., and Tong, M. J., "Mission Analysis and Aircraft Sizing of a Hybrid-Electric Regional Aircraft," *54th AIAA Aerospace Sciences Meeting 2016*, Curran Associates Inc, Red Hook, NY, 2016. https://doi.org/10.2514/6.2016-1028.

[8] Della Vecchia, P., Stingo, L., Nicolosi, F., de Marco, A., Cerino, G., Ciampa, P. D., Prakasha, P. S., Fioriti, M., Zhang, M., Mirzoyan, A., Aigner, B., and Charbonnier, D., "Advanced turboprop multidisciplinary design and optimization within AGILE project," *18th AIAA Aviation Technology, Integration, and Operations Conference 2018*, Curran Associates Inc, Red Hook, NY, 2018. https://doi.org/10.2514/6.2018-3205.

[9] Geiselhart, K. A., "A Technique for Integrating Engine Cycle and Aircraft Configuration Optimization," , 1994.

[10] Patnaik, S. N., Lavelle, T. M., Hopkins, D. A., and Coroneos, R. M., "Cascade Optimization Strategy for Aircraft and Air-Breathing Propulsion System Concepts," *Journal of Aircraft*, Vol. 34, No. 1, 1997, pp. 136–139. https://doi.org/10.2514/2.2148.

[11] Rallabhandi, S. K., and Mavris, D. N., "Simultaneous Airframe and Propulsion Cycle Optimization for Supersonic Aircraft Design," *Journal of Aircraft*, Vol. 45, No. 1, 2008, pp. 38–55. https://doi.org/10.2514/1.33183.

[12] Drela, M., "Simultaneous Optimization of the Airframe, Powerplant, and Operation of Transport Aircraft," , 2010. URL http://web.mit.edu/drela/Public/papers/RAeS/rt.pdf.

[13] Kestner, B. K., Schutte, J. S., Gladin, J. C., and Mavris, D. N., "Ultra High Bypass Ratio Engine Sizing and Cycle Selection Study for a Subsonic Commercial Aircraft in the N+2 Timeframe," *American Society of Mechanical Engineers, International Gas Turbine Institute 2011 – Proceedings of the ASME Turbo*, 2011, pp. 127–137. https://doi.org/10.1115/GT2011-45370.

[14] Kestner, B., Schutte, J. S., Tai, J. C. M., Perullo, C. A., and Mavris, D. N., "Surrogate Modeling for Simultaneous Engine Cycle and Technology Optimization for Next Generation Subsonic Aircraft," *Proceedings of the ASME Turbo Expo 2012*, ASME, New York, N.Y, 2012, pp. 133–145. https://doi.org/10.1115/GT2012-68724.

[15] Berton, J. J., and Guynn, M. D., "Multi-Objective Optimization of a Turbofan for an Advanced, Single-Aisle Transport," *Journal of Aircraft*, Vol. 48, No. 5, 2011, pp. 1795–1805. https://doi.org/10.2514/1.C031333.

[16] Lammen, W., Kupijai, P., Kickenweitz, D., and Laudan, T., "Integrate engine manufacturer's knowledge into the preliminary aircraft sizing process," *Aircraft Engineering and Aerospace Technology*, Vol. 86, No. 4, 2014, pp. 336–344. https://doi.org/10.1108/AEAT-10-2012-0190.

[17] Seitz, A., "Advanced Methods for Propulsion System Integration in Aircraft Conceptual Design," Dissertation, Technische Universität München, München, 2012.

[18] Häßy, J., Schmeink, J., Becker, R., Reitenbach, S., Vieweg, M., Bekemeyer, P., and Merle, A., "Hybrid Surrogate-Based Rubber Engine Model for Aircraft Multidisciplinary Design Optimization," *AIAA AVIATION 2020 FORUM*, American Institute of Aeronautics and Astronautics, Reston, Virginia, 06152020. https://doi.org/10.2514/6.2020-3186.

[19] Di Stasio, M., Trifari, V., Nicolosi, F., de Marco, A., and Schaber, R., "Bypass Ratio Parametric Analyses on a Narrow-Body Aircraft Using a New Tool for Turbofan Rubberization," *AIAA AVIATION 2022 Forum*, American Institute of Aeronautics and Astronautics, Reston, Virginia, 06272022. https://doi.org/10.2514/6.2022-3289.

[20] Becker, R.-G., Reitenbach, S., Klein, C., Otten, T., Nauroz, M., and Siggel, M., "An Integrated Method for Propulsion System Conceptual Design," *Proceedings of the ASME Turbo Expo: Turbine Technical Conference and Exposition - 2015*, ASME, New York, NY, 2015. https://doi.org/10.1115/GT2015-43251.

[21] Reitenbach, S., Krumme, A., Behrendt, T., Schnös, M., Schmidt, T., Hönig, S., Mischke, R., and Mörland, E., "Design and Application of a Multidisciplinary Predesign Process for Novel Engine Concepts," *Journal of Engineering for Gas Turbines and Power*, Vol. 141, No. 1, 2019. https://doi.org/10.1115/1.4040750.

[22] Reitenbach, S., Vieweg, M., Becker, R., Hollmann, C., Wolters, F., Schmeink, J., Otten, T., and Siggel, M., "Collaborative Aircraft Engine Preliminary Design using a Virtual Engine Platform, Part A: Architecture and Methodology," *AIAA Scitech 2020 Forum*, American Institute of Aeronautics and Astronautics, Reston, Virginia, 01062020. https://doi.org/10.2514/6.2020-0867.

[23] Häßy, J., and Schmeink, J., "Knowledge-Based Conceptual Design Methods for Geometry and Mass Estimation of Rubber Aero Engines," *ICAS 2022 - 33rd Congress of the International Council of the Aeronautical Sciences*, 2022. URL https://elib.dlr.de/192376/.

[24] Häßy, J., Becker, R.-G., and Bolemant, M., "An Educated Guess - Predicting Turbomachinery Efficiencies of Aero Engines During Conceptual Design," *GT2023-103638, Proceedings of the ASME Turbo Expo 2023*, 2023 (forthcoming).

[25] EASA, "Type-Certificate Data Sheet No. IM.E.093: PW1100G-JM Series Engines," , 2019.

[26] "ICAO Aircraft Engine Emissions Databank," , 2021. URL https://www.easa.europa.eu/domains/environment/icao-aircraft-engine-emissions-databank#group-easa-downloads.

[27] Kurzke, J., "Fundamental Differences Between Conventional and Geared Turbofans," *Proceedings of the ASME Turbo Expo 2009*, ASME, New York, NY, 2009, pp. 145–153. https://doi.org/10.1115/GT2009-59745.

[28] Grieb, H. (ed.), *Projektierung von Turboflugtriebwerken*, Technik der Turboflugtriebwerke, Birkhäuser Basel, Basel and s.l., 2004. https://doi.org/10.1007/978-3-0348-7938-5.

[29] Wehrel, P., "Technological Level of CMC Components for Stationary Gas Turbines and Aero-Engines: DLR Report," , ???? URL https://elib.dlr.de/186166/.

[30] Pera, R. J., Onat, E., Klees, G. W., and Tjonneland, E., "A Method to Estimate Weight and Dimensions of Aircraft Gas Turbine Engines: Volume I: Method of Analysis," , 1977.

[31] Klees, G. W., and Fishbach, L. H., "Aircraft Engine Weight Estimation Method," *Thirty-Seventh Annual Conference*, edited by Society of Allied Weight Engineers, Inc., 1978.

[32] Bretschneider, S., "Knowledge-Based Preliminary Design of Aero-Engine Gas-Generators," Dissertation, Universität Stuttgart, Stuttgart, 2011. URL dissertation.de.

[33] McKinney, R., Cheung, A., Sowa, W., and Sepulveda, D., "The Pratt & Whitney TALON X Low Emissions Combustor: Revolutionary Results with Evolutionary Technology," *Aerospace Sciences Meetings*, 2007. https://doi.org/10.2514/6.2007-386.

[34] Madden, P., and Park, K., "Methodology for Predicting NOx Emissions at Altitude Conditions from Ground Level Engine Emissions and Performance Test Information," , 2003.

[35] Stöppler, B., "Entwicklung einer verbesserten Korrelation für die Stickoxidemission von Flugtriebwerken," , 1992.

[36] Döpelheuer, A., "Anwendungsorientierte Verfahren zur Bestimmung von CO, HC und Ruß aus Luftfahrttriebwerken," Dissertation, Ruhr-Universität Bochum, Bochum, 2002. URL https://elib.dlr.de/49148/.

[37] Fröhler, B., Häßy, J., and Abu-Zurayk, M., "Development of a Medium/Long-Haul Reference Aircraft," *Deutscher Luft- und Raumfahrtkongress 2022*, 2022.

[38] Bureau of Transportation Statistics, "Air Carrier Statistics Database: T-100 Segment (All Carriers)," , 2023. URL https://www.transtats.bts.gov/Tables.asp?QO_VQ=EEE&QO_anzr=Nv4%FDPn44vr4%FDf6n6v56vp5%FD%FLS14z%FDHE%FDg4nssvp%FM-%FDNyy%FDPn44vr45&QO_fu146_anzr=Nv4%FDPn44vr.

[39] Seider, D., Fischer, P. M., Litz, M., Schreiber, A., and Gerndt, A., "Open source software framework for applications in aeronautics and space," *2012 IEEE Aerospace Conference*, IEEE, 2012. https://doi.org/10.1109/aero.2012.6187340.

[40] Nagel, B., Böhnke, D., Gollnick, V., Schmollgruber, P., Rizzi, A., Rocca, G. L., and Alonso, J. J., "Communication in Aircraft Design: Can we establish a Common Language?" *ICAS*, 2012. URL https://elib.dlr.de/134586/.

[41] Alder, M., Moerland, E., Jepsen, J., and Nagel, B., "Recent Advances in Establishing a Common Language for Aircraft Design with CPACS," *Aerospace Europe Conference 2020*, 2020. URL https://elib.dlr.de/134341/.

[42] Wöhler, S., Atanasov, G., Silberhorn, D., Fröhler, B., and Zill, T., "Preliminary Aircraft Design within a Multidisciplinary and Multifidelity Design Environment," *Aerospace Europe Conference 2020*, 2020.

[43] Horstmann, K. H., "Ein Mehrfach-Traglinienverfahren und seine Verwendung für Entwurf und Nachrechnung nichtplanarer Flügelanordnungen," Tech. rep., Deutsches Zentrum für Luft- und Raumfahrt e.V, 1987.

[44] Torenbeek, E., *Synthesis of Subsonic Airplane Design*, Springer Netherlands, 2013. URL https://www.ebook.de/de/product/25435562/e_torenbeek_synthesis_of_subsonic_airplane_design.html.

[45] Raymer, D. P., *Aircraft Design: A Conceptual Approach (AIAA Education Series)*, American Institute of Aeronautics & Astronautics; 6. Edition, 2018.

[46] Dallara, E. S., "Aircraft design for reduced climate impact," Ph.D. thesis, Stanford University, 2011. URL https://purl.stanford.edu/yf499mg3300.

[47] Thorbeck, J., "From Aircraft Performance to Aircraft Assessment," Tech. rep., Technische Universität Berlin, 2007.

[48] Han, Z.-H., and Görtz, S., "Hierarchical Kriging Model for Variable-Fidelity Surrogate Modeling," *AIAA Journal*, Vol. 50, No. 9, 2012, pp. 1885–1896. https://doi.org/10.2514/1.J051354.

[49] Franz, T., Zimmermann, R., Görtz, S., and Karcher, N., "Interpolation-based reduced-order modelling for steady transonic flows via manifold learning," *International Journal of Computational Fluid Dynamics*, Vol. 28, No. 3-4, 2014, pp. 106–121. https://doi.org/10.1080/10618562.2014.918695.

[50] Ripepi, M., Verveld, M. J., Karcher, N. W., Franz, T., Abu-Zurayk, M., Görtz, S., and Kier, T. M., "Reduced-order models for aerodynamic applications, loads and MDO," *CEAS Aeronautical Journal*, Vol. 9, No. 1, 2018, pp. 171–193. https://doi.org/10.1007/s13272-018-0283-6.